Journal of Molecular and Cellular Cardiology 94 (2016) 54–64

Contents lists available at ScienceDirect

Journal of Molecular and Cellular Cardiology

journal homepage: www.elsevier.com/locate/yjmcc

Prolongation of atrio-ventricular node conduction in a rabbit model of ischaemic cardiomyopathy: Role of fibrosis and connexin remodelling

Ashley M. Nisbet [a,1], Patrizia Camelliti [b,*,1], Nicola L. Walker [a], Francis L. Burton [a], Stuart M. Cobbe [a], Peter Kohl [c,d], Godfrey L. Smith [a,*]

[a] British Heart Foundation Glasgow Cardiovascular Research Centre, University of Glasgow, Glasgow G12 8QQ, UK
[b] School of Biosciences and Medicine, University of Surrey, Guildford, GU2 7XH, UK
[c] Institute for Experimental Cardiovascular Medicine, University Heart Centre Freiburg - Bad Krozingen, Medical School of the University of Freiburg, Germany
[d] Heart Science Centre, National Heart and Lung Institute, Imperial College London, Harefield UB9 6JH, UK

ARTICLE INFO

Article history:
Received 17 November 2015
Received in revised form 16 March 2016
Accepted 23 March 2016
Available online 25 March 2016

Keywords:
Myocardial infarction
Heart failure
Left ventricular dysfunction
Conduction
Optical mapping
Connexins

ABSTRACT

Conduction abnormalities are frequently associated with cardiac disease, though the mechanisms underlying the commonly associated increases in PQ interval are not known. This study uses a chronic left ventricular (LV) apex myocardial infarction (MI) model in the rabbit to create significant left ventricular dysfunction (LVD) 8 weeks post-MI. *In vivo* studies established that the PQ interval increases by approximately 7 ms (10%) with no significant change in average heart rate. Optical mapping of isolated Langendorff perfused rabbit hearts recapitulated this result: time to earliest activation of the LV was increased by 14 ms (16%) in the LVD group. Intra-atrial and LV transmural conduction times were not altered in the LVD group. Isolated AVN preparations from the LVD group demonstrated a significantly longer conduction time (by approximately 20 ms) between atrial and His electrograms than sham controls across a range of pacing cycle lengths. This difference was accompanied by increased effective refractory period and Wenckebach cycle length, suggesting significantly altered AVN electrophysiology post-MI. The AVN origin of abnormality was further highlighted by optical mapping of the isolated AVN. Immunohistochemistry of AVN preparations revealed increased fibrosis and gap junction protein (connexin43 and 40) remodelling in the AVN of LVD animals compared to sham. A significant increase in myocyte–non-myocyte connexin co-localization was also observed after LVD. These changes may increase the electrotonic load experienced by AVN muscle cells and contribute to slowed conduction velocity within the AVN.

1. Introduction

The prognosis in chronic heart failure (CHF) is affected by conduction abnormalities in both the atrio-ventricular node (AVN) and the His-Purkinje system in approximately 50% of patients [1–5]. Atrio-ventricular and intra-ventricular conduction changes can produce adverse haemodynamic effects *via* their impact on left ventricular (LV)/right ventricular (RV) synchrony and ventricular contraction-relaxation sequence. Slower atrio-ventricular conduction manifests itself on the surface electrocardiogram (ECG) *via* a prolonged PR interval. This leads to delayed ventricular activation which may be sufficient to cause pre-systolic mitral regurgitation, reducing LV preload and, hence, output. Multisite biventricular pacing techniques (also known as cardiac resynchronisation therapy) improve cardiac hemodynamic function by correcting LV and RV activation times [6–8]. Further improvements in systolic function can be achieved by optimisation of preload by correct timing of atrio-ventricular delay [2,9,10]. The causes and mechanisms of abnormal conduction are not known. In particular, whether a specific site in the conduction system is involved, and whether the effect is a direct or indirect consequence of a pathological change, are open questions. That said, a recent publication reported both structural and molecular changes within the AVN of a rabbit model of cardiac hypertrophy [11], suggesting that this tissue region may be causally involved.

Physiological conduction in the AVN is already slow, compared to atrial and ventricular myocardium, due to distinct electrical properties of AVN tissue, including significantly different expression levels of a range of ion channels, including connexins [12]. The mammalian heart contains three main connexin isoforms: connexin43 (Cx43), connexin40 (Cx40) and connexin45 (Cx45). There is heterogeneous expression of all three isoforms within the tissue of the Triangle of Koch [13]. The most abundant cardiac connexin, Cx43, has major roles in

Abbreviations: AVN, atrio-ventricular node; AN, atrio-nodal; CHF, chronic heart failure; ERP_A, atrial effective refractory period; ERP_{AVN}, AVN effective refractory period; FRP_{AVN}, AVN functional refractory period; LV, left ventricle; LVD, left ventricular dysfunction; MI, myocardial infarction; NH, nodo-Hisian; O/N, overnight; RV, right ventricle; RT, room temperature; Tact, activation time.

* Corresponding authors.
E-mail address: p.camelliti@surrey.ac.uk (P. Camelliti).
[1] These authors contributed equally to this work.

http://dx.doi.org/10.1016/j.yjmcc.2016.03.011

cell-cell communication of working ventricular and atrial myocytes. It shows relatively low expression within the compact AVN, but is observed in the transitional zones of the atrio-nodal (AN) and nodo-Hisian (NH) regions. The posterior nodal extension has the lowest Cx43 mRNA and the most abundant HCN4 mRNA levels, in keeping with its low conduction velocity and secondary pacemaker activity [14]. In contrast, the low-conductivity Cx45 has been shown to be abundant in the compact node, and both Cx40 and Cx45 have been reported in the NH region [15–17].

The mechanisms underlying abnormal delays in atrio-ventricular conduction in CHF are not fully understood. This study therefore aims to assess atrio-ventricular conduction delay in a rabbit model of left ventricular dysfunction (LVD) due to apical myocardial infarction (MI), and to investigate possible mechanisms underlying this delay. Our results indicate that the significantly longer PQ interval, observed in this rabbit model of LVD, is due to abnormally slow conduction through the compact AVN. The increase in conduction time is associated with fibrosis, higher non-myocyte content and altered expression of connexins in the AVN, possibly including hetero-typic cell coupling, as part of the structural remodelling following MI.

2. Methods

2.1. Animal model

Procedures were undertaken in accordance with the United Kingdom Animals (Scientific Procedures) Act of 1986 and conform to the Guide for the Care and Use of Laboratory Animals published by the US National Institutes of Health (NIH Publication No. 85–23, revised 1996). A well-characterised model of MI, induced by coronary artery ligation, was used [18–24]. In short, adult male New Zealand White rabbits (2.5–3.0 kg) were given premedication with 0.4 mL/kg intramuscular Hypnorm (fentanyl citrate, 0.315 mg/mL: fluanisone 10 mg/mL, Janssen Pharmaceuticals). Anaesthesia was induced with 0.25–0.5 mg/kg midazolam (Hypnovel, Roche) given *via* an indwelling cannula in the marginal ear vein. Rabbits were intubated and ventilated using a Harvard small animal ventilator with a 1:1 mixture of nitrous oxide and oxygen containing 1% halothane at a tidal volume of 50 mL and a frequency of 40 min^{-1}. Preoperative antibiotic prophylaxis was given with 1 mL Amfipen (ampicillin 100 mg/mL, Mycofarm UK Ltd) intramuscularly. A left thoracotomy was performed through the 4^{th} intercostal space. Quinidine hydrochloride (10 mg/kg; Sigma Pharmaceuticals), a class IA antiarrhythmic (potassium channel blocker) was administered intravenously prior to coronary artery ligation to reduce the incidence of ventricular fibrillation. The marginal branch of the left circumflex coronary artery, which supplies most of the LV free wall, was ligated halfway between the atrio-ventricular groove and the cardiac apex to produce an ischaemic area of 30–40% of the LV. As there is relatively little collateral circulation in the rabbit, a relatively uniform apical MI was produced transmurally, occupying on average 14% of the total endocardial and epicardial surfaces of the LV (Fig 1A(i)) [18]. Sham controls did not undergo coronary artery ligation, but were subjected to all other interventions.

2.2. Characterisation of the rabbit model of LVD

Rabbits were sedated with 0.3 mg/kg Hypnorm prior to echocardiography and ECG. Echocardiographic assessment of LV end-diastolic dimension and systolic function was performed at 7 weeks post coronary artery ligation or sham operation, using a 5 MHz paediatric probe with a Toshiba sonograph (Sonolayer 100). The ECG was measured to determine RR and PQ intervals, and QS and QT durations in the intact animal, and to identify any effect of LVD on these parameters. PQ and QS intervals were reported instead of PR in an attempt to assess the contribution of ventricular conduction time separately from atrial and AVN conduction. To record high quality ECG signals, three electrodes were positioned subcutaneously, and the ECG recorded from lead II. Increased inducibility of arrhythmias and lowered ventricular fibrillation threshold were further assessed after organ isolation, *ex vivo*, 8 weeks after the initial surgery [18].

This study describes investigations both *in vivo* and *in vitro*. Three distinct *in vitro* studies were performed: (i) optical measurements on isolated whole hearts (8 sham and 8 LVD preparations); (ii) extracellular electrode measurements on isolated AVN preparations (14 sham and 14 LVD); (iii) optical measurements on isolated AVN preparations (4 sham and 4 LVD). In a separate set of experiments, ECG measurements were made on sham and LVD rabbit groups as described above (8 sham and 8 LVD animals). Accumulated mortality statistics, excluding mortality associated with the operative procedure, were collected over approximately 20 years of studies using the rabbit MI model (499 LVD and 303 sham procedures).

2.3. Whole heart optical mapping studies

Eight weeks after surgery, rabbits (8 LVD, 8 sham controls) were sacrificed with an intravenous injection of 0.5 mL/kg Euthatal (sodium pentobarbitone 200 mg/kg, Rhone Merieux), mixed with 500 IU of heparin. Hearts were rapidly excised and Langendorff-perfused with oxygenated Tyrode's solution (containing in mmol/L: NaCl 93, $NaHCO_3$ 20, Na_2HPO_4 1.0, $MgSO_4$ 1.0, KCl 5.0, $CaCl_2$ 1.8, Na-acetate 20, and glucose 20; equilibrated with 95% O_2/5% CO_2, pH 7.4.) at 37 °C and at constant rate of 40 mL/min using a Gilson Minipuls 3 peristaltic pump. Perfusion pressure was monitored with a transducer in the aortic cannula. A pair of platinum stimulation electrodes was placed in the low right atrium. Hearts were loaded with a bolus injection (200 μL injected into the perfusate over 30 s, *i.e.* diluted in 20 mL of saline) of the voltage sensitive dye RH237 (Molecular Probes, OR USA) dissolved in DMSO (1 mg/mL). For optical mapping recordings, hearts were placed in a custom-built chamber which allowed control of bathing solution temperature and recording of global ECG *via* wall-fixed electrodes (Fig. 2A). The anterior surface of the heart was illuminated by 535 ± 25 nm light (interference filter, Comar Instruments Ltd, UK) from four 100 W tungsten-halogen lamps. Light emitted from the heart was collected using a camera lens (Nikon 85 mm, NA 1.4), passed through a 695 nm long-pass filter (Omega Optical Inc, USA) and focused onto a 16 × 16 photodiode array (C4675-102, Hamamatsu Photonics UK Ltd). Images were collected at 1 kHz from an area of 15 × 15 mm, saved to computer disk, and analyzed using custom software following application of a Gaussian spatial filter (radius 2 pixels) in accordance with the principles set out in Mironov et al. [25]. Artefacts in electric recordings, caused by motion, were reduced with 3 μmol/L cytochalasin-D (Sigma Aldrich, UK), which we previously found to have no significant effects on cardiac activation parameters in rabbits over the range of stimulus frequencies used in this study [26].

Isochronal maps of activation time were constructed, and conduction velocity was derived. The range of activation times in a given heart under specific pacing conditions was defined as the difference in timing between the earliest and latest action potential upstroke recorded by the photodiode array.

Transmural conduction through the LV free wall was assessed by pacing from the ventricular endocardium *via* a plunge bipolar electrode and monitoring earliest LV epicardial activation using optical mapping. LV longitudinal conduction velocity was assessed by pacing from the LV epicardium and monitoring optical signals at a 5 mm radius from the activation point.

2.4. Isolated AVN preparation functional studies

In a separate set of experiments, isolated AVN preparations (14 sham and 14 LVD) were prepared by the removal of all ventricular tissue, followed by an incision around the crest of the right atrial appendage which, when folded open, exposed the endocardial surface of the

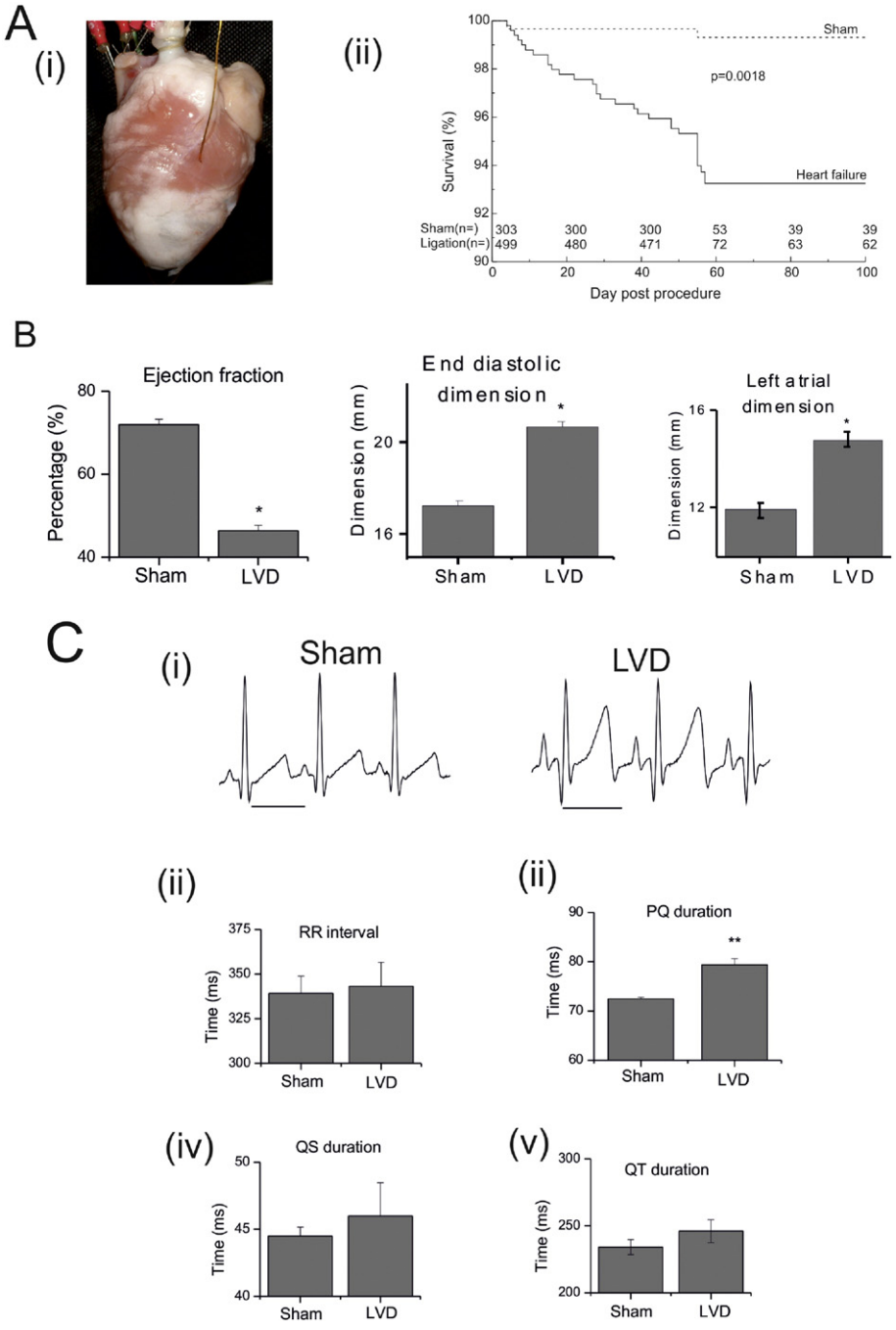

Fig. 1. *In vivo* parameters from the rabbit model of LVD. A: (i) Photograph of the Langendorff perfused rabbit heart showing the apical MI scar. (ii) Kaplan-Meier plot of survival in LVD (ligation) *versus* sham showing increased mortality in LVD. $p = 0.0018$, data accumulated over several studies. B: Graphs of LV ejection fraction (expressed as a percentage), LV end-diastolic dimension (in mm) and left atrial dimension (in mm). Results expressed as mean ± SEM; 8 sham/8 LVD animals. C: (i) Examples of surface ECG recordings *in vivo*. Scale bar: 250 ms. (ii–v) Graph of RR, PQ, QS and QT intervals (in ms). Results expressed as mean ± SEM; $n = 8$ sham/$n = 8$ LVD.

right atrium and inter-atrial septum. Remaining left atrial tissue was removed, leaving a section of tissue containing the Triangle of Koch, the *Crista terminalis*, and the right atrial appendage (Fig. 3A). The sinus node was left intact. This preparation was pinned onto a Sylgard plate, carefully avoiding excess deformation, and superfused with oxygenated Tyrode's solution (40 mL/min, 37 °C). A bipolar silver wire stimulating electrode was positioned on the endocardium at the right atrial appendage near the sinus node. The spontaneous sinus cycle length was recorded in every experiment. Thereafter, the atrium was paced using 2 ms voltage pulses with amplitude of twice the threshold. Two silver wire bipolar extracellular recording electrodes monitored surface electrograms from the low inter-atrial septum and the His bundle region; the inter-electrode distance was fixed at 14 mm. Electrograms were high pass (40 Hz) filtered by the MAP amplifier before digitization.

Rate-dependent properties of the AVN were determined by standard pacing protocols. The interval between late atrial activation and His bundle activation (AH interval) and Wenckebach cycle length (*i.e.* cycle length at which atrio-ventricular block occurred) were derived using 16 stimuli at the basic cycle length of 300 ms followed by a 1 s pause, with the cycle length decrementing by 5 ms intervals after each pause. The atrial effective refractory period (ERP_A) was defined as the longest interval of a test sino-atrial node stimulus pulse (S1S2 interval) that failed to elicit a corresponding atrial electrogram (A2 response), and was determined using a protocol that consisted of 16 beats at the

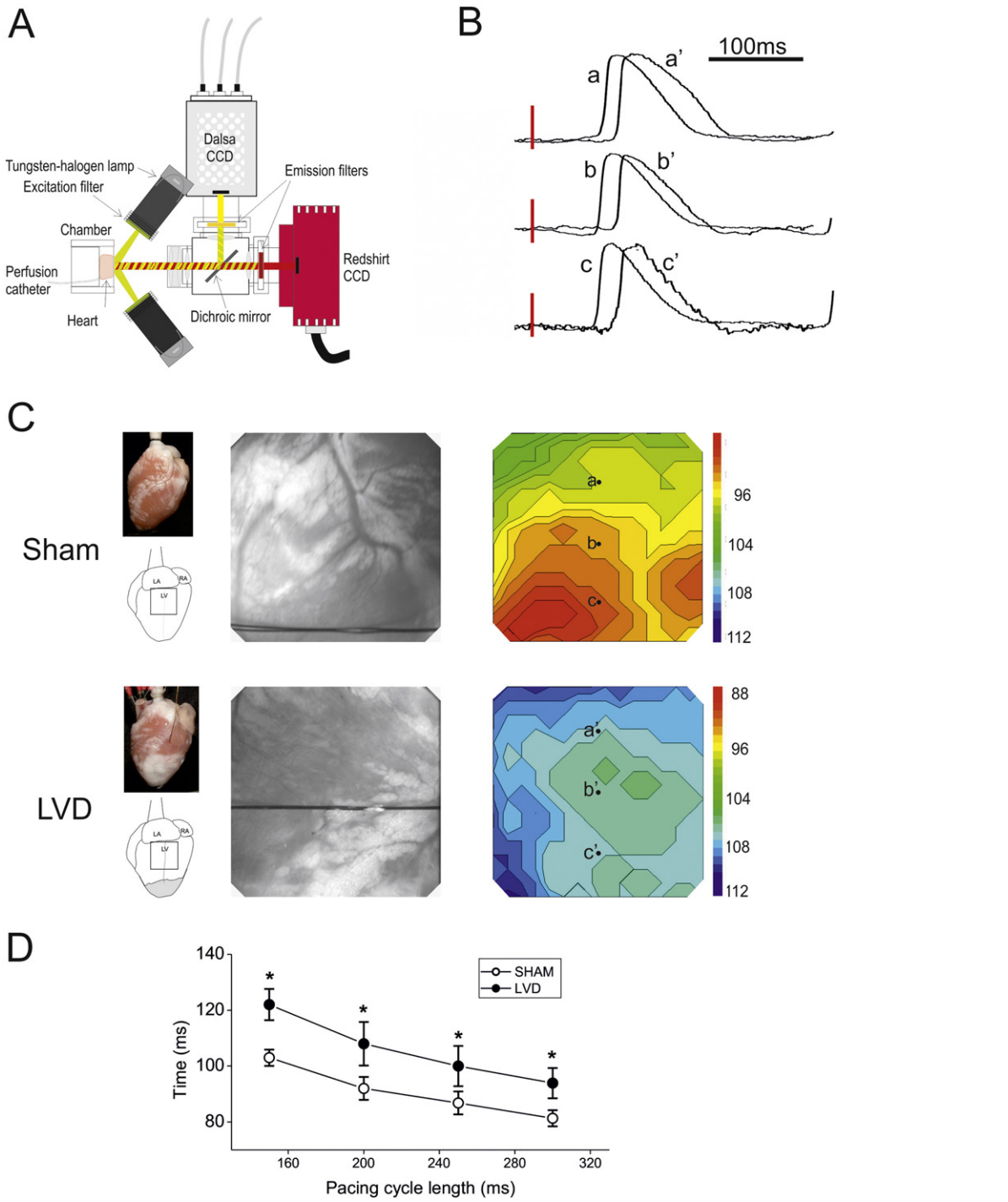

Fig. 2. Optical measurements of epicardial activation time. A: Schematic diagram of the optical mapping apparatus (CCD – charged coupled device). B: Examples of optically derived action potentials at 3 points on the surface of the left ventricle. Traces a, b, and c originate from sham controls. Traces a, b and c originate from the LVD model. Timing is measured relative to the right atrial stimulus artefact (red vertical line). C: Isochronal maps of epicardial activation time relative to right atrial stimulus in sham and LVD. Photographs and schematic drawing illustrate the area optically imaged (LV). Epicardial activation time (in [ms]) shown on the right of the isochronal maps. Isochrones show activation times early (red) to late (blue). D: Graph of the time to earliest epicardial activation from right atrial pacing against pacing cycle length (in ms). Mean ± SEM, $n = 8$ sham, $n = 8$ LVD preparations. $^{*}p < 0.05$.

basic pacing cycle length (PCL) followed by one premature beat followed by a 1 s pause. The premature beat coupling interval was decremented by 5 ms steps until atrial refractoriness occurred. The AVN ERP (ERP_{AVN}) is defined as the longest interval for a test atrial stimulus (A1A2 interval) that failed to elicit a test His bundle response (H2 response). The AVN functional refractory period (FRP_{AVN}) is defined as the shortest interval between His electrogram from the standard stimulus and the His electrogram from the test stimulus (H1H2 interval) achieved by premature stimulation. These protocols allow atrioventricular conduction and refractoriness curves to be constructed, from which parameters of AVN function can be derived.

The sequence of activation through the AVN in the isolated AVN preparation was additionally studied in 4 sham and 4 LVD AVN preparations using optical mapping. For this, excised hearts were first loaded with RH237 as described above. The AVN was then isolated (prepared as described above) and mounted in a custom-made chamber to allow

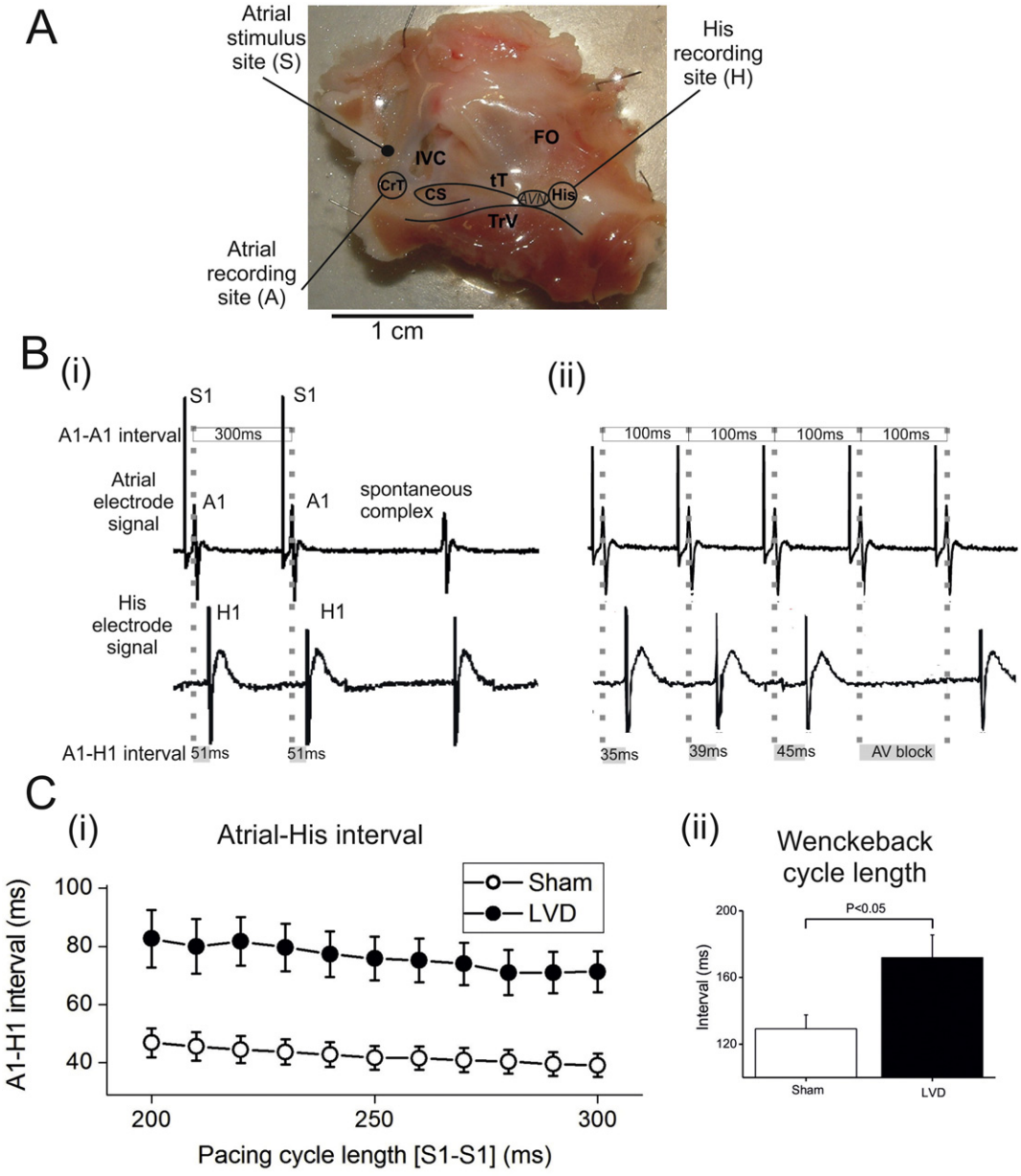

Fig. 3. Electrical characteristics of the isolated AVN (i). A: Photograph of the isolated AVN preparation. Anatomical landmarks are annotated. (IVC – inferior vena cava; FO – fossa ovalis; CrT – Crista terminalis; tT – tendon of Todaro; CS – coronary sinus; TrV – tricuspid valve; His – His bundle recording site; AVN – compact AV nodal region). B: (i) Surface electrograms from the isolated AVN preparation showing how the time between atrial and His bundle electrograms (A1H1 time) are derived by measurement of the interval between the onset of the atrial signal to the onset of the corresponding His bundle electrogram. (ii) Atrial and His bundle electrograms demonstrating progressive prolongation of the A1H1 interval and then conduction block, *i.e.* Wenckebach conduction block. C: (i) Graph of A1H1 intervals against pacing cycle length (in ms) in sham and LVD animals. (ii) Wenckebach cycle length (in ms). Mean ± SEM, $n = 14$ sham, $n = 14$ LVD preparations.

superfusion with Tyrode's solution and simultaneous recording of surface electrograms and optically derived action potentials using a Redshirt Imaging (USA) CCD array. The image of the AVN was focused onto the array such that an area of (14.5×14.5) mm^2 at a spatial resolution of 40×40 pixels (3 kHz frame rate) was imaged. The preparation was paced using the protocols described above.

2.5. Connexin expression and distribution and fibrosis quantification in isolated AVN preparations

Following functional studies, isolated AVN preparations (7 sham and 7 LVD) were embedded flat in Tissue-Tek (VWR International Ltd) and rapidly frozen in liquid nitrogen following the protocol described previously [27]. Cryosections (16 μm) were cut in the plane of the AVN preparation, collected on SuperFrost slides (Menzel-Glaser, Germany) and stored at −80 °C until use. For immunolabelling [28], cryosections were fixed in cold acetone (10 min), washed with phosphate buffered saline (PBS), and blocked for 1 h at room temperature (RT) in 1% bovine serum albumin in PBS containing 0.1% TritonX-100. Gap junction proteins Cx40 and Cx43 were labelled using goat Cx40 or Cx43 antibodies (Santa Cruz Biotechnology; 1:200, overnight (O/N) at 4 °C), followed by the secondary donkey anti-goat Alexa488 (1:500, 2 h RT; Molecular Probes). Myocytes were labelled with a mouse anti-myomesin antibody (clone B4; kindly supplied by Dr H.M. Eppenberger, ETH Zürich, Switzerland; 1:100, O/N at 4 °C), followed by donkey anti-mouse CY3 (1:400, 2 h RT; Jackson Immuno Research Laboratories). Non-myocytes were identified using a mouse monoclonal anti-vimentin antibody (clone V9, Sigma Aldrich; 1:1000, 2 h RT) pre-conjugated with Alexa647 using a Molecular Probes' Zenon immunolabelling kit (Molecular Probes). The mouse monoclonal anti-neurofilament 160 antibody

(NF160; Chemicon; 1:1000, O/N at 4 °C) was used to identify the compact AVN region. All immuno-labelled cryosections were mounted in CitiFluor antifade medium (Agar Scientific, UK), and imaged with a TCS-SP2 confocal laser-scanning microscope (Leica Microsystems, Germany) using 488 nm excitation and 500–535 nm emission for Alexa488 labelling, 543 nm excitation and 555–630 nm emission for CY3 labelling, and 633 nm excitation and 650–750 nm emission for Alexa647 labelling. Single optical slices or z-series were recorded and images were combined to reveal localization of connexins to myocytes and non-myocytes.

For connexin quantification, single optical slice images showing Cx40 or Cx43 immunolabelling, together with myocyte and non-myocyte immunolabelling, were quantitatively analyzed using ImageJ (http://rsb.info.nih.gov/ij/). Co-localization of connexin fluorescence spots with cell labelling (myocytes or non-myocytes) was used to identify cell-type specific expression levels. Connexin density is stated as (i) area of connexin-related fluorescence per total tissue area, (ii) area of connexin-related fluorescence per cell-type relative to total scanned tissue area, and (iii) percentage of connexin expressed by myocytes and non-myocytes relative to total connexin area.

Fibrosis was detected using picrosirius red staining. Briefly, cryosections were fixed in formol calcium (5 min), washed in tap water, incubated in picrosirius red (3 min at RT), rinsed in absolute alcohol, cleared and mounted in DPX. Stained cryosections were imaged with a Zeiss Axioskope equipped with a Nikon DMX1200F digital camera. Fibrosis was quantified as percentage area of picrosirius red per total tissue area.

2.6. Statistical analysis

Data are expressed as mean ± SEM. Statistical analyses were performed using Student's *t*-test or analysis of variance. The criterion for statistical significance was $p < 0.05$.

3. Results

3.1. Characteristics of LVD in the rabbit model of heart failure

Coronary ligated rabbits showed significant haemodynamic dysfunction, including increased LV end-diastolic dimensions and decreased ejection fraction compared to sham-operated controls (Fig. 1B). The surgical model was also associated with significant late mortality as illustrated by the Kaplan Meier graph (Fig. 1A(ii); $p = 0.0018$) based on data accumulated over a series of studies from our laboratory [21,22,26,29–33].

Fig. 1C shows representative surface ECG recordings from sham control and LVD animals. There was significant prolongation of the PQ interval in LVD animals, compared to controls (Sham 72.5 ± 0.3 ms; LVD 79.4 ± 1.2 ms, $n = 8$ $p < 0.05$), but no significant difference in the other ECG parameters (RR interval: 339.2 ± 9.7 ms *vs.* 343.1 ± 13.5 ms, $p > 0.05$; QS interval: 44.5 ± 0.7 ms *vs.* 46.0 ± 2.5 ms, $p > 0.05$) or QT interval 234.1 ± 6.6 ms *vs.* 246.0 ± 8.5 ms, $p > 0.05$).

3.2. Optical measurements of epicardial activation time in the intact heart

Epicardial activation during atrial pacing in sham and LVD Langendorff-perfused rabbit hearts is shown in Fig. 2. Photographs of the LV epicardial surface with corresponding isochronal maps of activation are illustrated in Fig. 2C. Sample optical action potentials measured at 3 points on the epicardial surface of sham and LVD hearts are shown in Fig. 2B. These signals were used to examine the time and pattern of epicardial activation. As indicated in Fig. 2C, the time for earliest LV activation was delayed in LVD hearts, compared to the sham group. During atrial pacing at a cycle length of 250 ms, the interval between right atrial stimulation and first LV epicardial activation was 14 ± 3 ms (16 ± 2%) greater in LVD hearts than in sham. Fig. 2D shows that this effect was rate dependent, with higher conduction delays at lower pacing cycle length.

Importantly, no increase in intra-atrial, LV transmural or LV epicardial conduction time was observed in LVD hearts (e.g. intra-atrial time: 18.8 ± 0.7 ms in LVD *vs.* 17.9 ± 0.8 ms sham, $n = 8$ each, $p > 0.5$; transmural time: 14.2 ± 2.2 ms in LVD *vs.* 14.5 ± 3.5 ms in sham, $n = 8$ each, $p > 0.5$), suggesting that the delay in LV activation was not due to intra-atrial or intra-ventricular conduction slowing. Therefore the increased time delay between atrial stimulation and the arrival of excitation at the LV epicardial surface in LVD is likely to result from slowed conduction inside the AVN.

3.3. Conduction slowing in isolated AVN preparations measured using extracellular electrodes

The effect of LVD on conduction inside the AVN was studied in a series of 14 sham and 14 LVD isolated AVN preparations. Fig. 3A shows the isolated AVN with anatomical landmarks annotated. Surface right atrial and His bundle electrograms are also shown (Fig. 3B). There was no significant difference in the spontaneous sinus cycle length between LVD and sham animals (LVD: 373.1 ± 23.2 ms, Sham: 378.1 ± 13.6 ms, $n = 14$ each; $p > 0.5$), which is in keeping with the *in vivo* data above (Fig. 1B(ii)). When the mean atrio-Hisian (A1H1) interval for each corresponding S1S1 interval was plotted, the value of the A1H1 interval was larger in LVD at all S1S1 intervals, resulting in an upward shift of the atrio-ventricular conduction curve, compared to sham (Fig. 3C(i)). Furthermore a significant prolongation of the Wenckebach cycle length was observed in LVD animals, compared to sham controls (Fig. 3C(ii)). Thus, consistent with the results obtained with intact animals and Langendorff-perfused hearts, LVD is associated with slowed conduction in the isolated AVN.

Effects of LVD on ERP_{AVN} and FRP_{AVN}, as well as on ERP_A, were derived using the pacing protocol described in the Methods. Results are shown in Fig. 4. ERP_A was not significantly altered in the LVD group compared to sham controls. However, there was a significant prolongation in ERP_{AVN} and FRP_{AVN} in LVD hearts, compared to sham controls.

In keeping with previous studies [34–36], we observed the presence of dual pathway AVN physiology in roughly a quarter of animals, based on the presence of discontinuity of the atrio-ventricular conduction curve, and functionally defined as an abrupt increase in the A2H2 interval of ≥20 ms in response to a 5 ms decrement in A1A2 (Supplemental Fig. S1A and B). Dual pathway AVN physiology could be identified in both sham controls (19.6%) and LVD (33.3%) animals, with no significant difference between the two groups (Chi-square, $p > 0.05$).

3.4. Atrio-ventricular conduction assessed by optical mapping of activation

The effect of LVD on atrio-ventricular conduction was monitored optically in a series of 4 sham and 4 LVD isolated AVN preparations loaded with the voltage-sensitive dye RH237, to determine directly the site showing the largest conduction slowing. Fig. 5 shows LVD effects on mean activation time (T_{act}) measured from optically derived action potentials. The data (Fig. 5) show that T_{act} is significantly longer in the compact AVN and His bundle regions in LVD *versus* controls (ANOVA $p < 0.001$), with no significant difference in T_{act} at the atrial and AVN input regions, consistent with the observation that LVD has no effect on intra-atrial conduction (see Langendorff-perfused hearts results). Conduction times between regions (ΔT_{act}) are shown in Fig. 5B. There is significant delay in conduction between the AVN input and compact AVN region in LVD, compared to sham (62 ± 14 ms in LVD *vs.* 16 ± 5 ms, $n = 4$ each, $p < 0.001$).

3.5. Fibrosis and alterations in connexin expression

Immunohistochemistry and histology of tissue sections prepared from isolated AVN preparations revealed the presence of fibrosis, higher

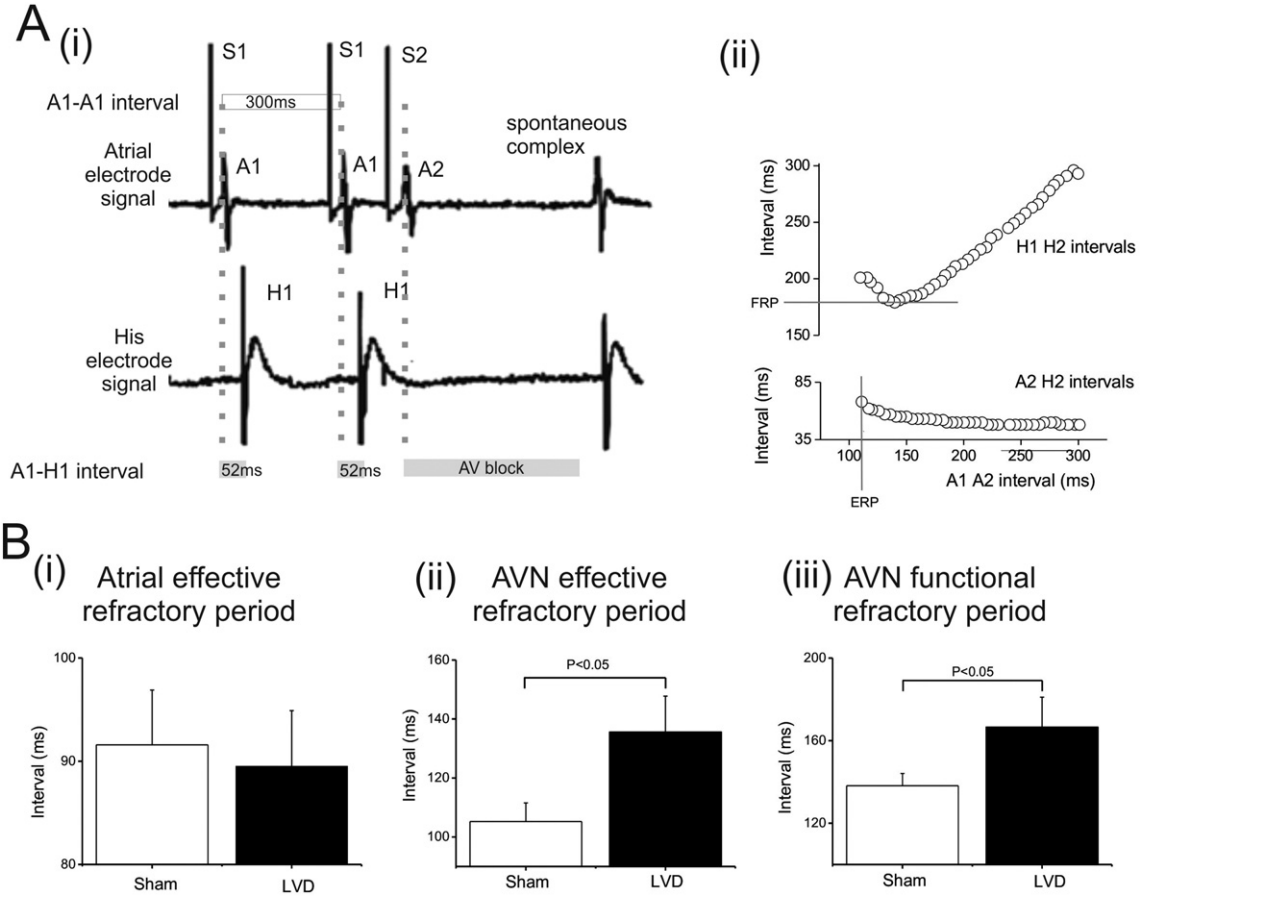

Fig. 4. Electrical characteristics of the isolated AVN (ii). A: Examples of atrial and His bundle electrograms during a premature stimulation pacing protocol. In this example AVN refractoriness is demonstrated by absence of the His bundle electrogram following the atrial signal (A2) from premature beat S2. AVN ERP is derived by plotting the A2H2 interval against the corresponding A1A2 interval; AV N FRP is derived by plotting the H1H2 interval against the corresponding A1A2 interval. B: Graphs of atrial effective refractory period, and AVN effective and functional refractory periods (in [ms]). Results expressed as mean ± SEM.

non-myocyte content and gap junction remodelling in both the compact AVN and atrio-nodal (AN) region of LVD animals compared to sham (Table 1, Fig. 6, Fig. S2). Fibrosis increased in the AN region and compact AVN (AN region: 20.8 ± 0.9% in LVD *vs.* 14.5 ± 0.9% of tissue area in sham animals, $n = 7$ each, $p = 0.0006$; compact AVN: 37.9 ± 1.3% in LVD *vs.* 26.6 ± 0.5% of tissue area in sham animals, $n = 7$ each, $p = 0.0006$), despite the fact that this tissue was distant from the (apically located) post-MI scar. Non-myocyte to myocyte area ratio increased significantly in the AN region from 0.18 ± 0.01 in control to 0.26 ± 0.02 in LVD ($p < 0.05$; $n = 7$), and in the compact AVN from 0.55 ± 0.03 in control to 0.75 ± 0.06 in LVD ($p < 0.05$; $n = 7$; compare panels on right to left in Fig. 6), indicating a net increase in non-myocyte content. Quantitative assessment of overall connexin protein showed an increase in Cx43 density in the AN region and a decrease in Cx40 density in both AN region and compact AVN in LVD rabbits compared to sham (Table 1, Fig. 6).

Triple labelling for connexins, myocytes and non-myocytes allowed connexin expression to be related to underlying cell types. Myocyte Cx43 levels did not change in AN myocytes, but a significant increase in Cx43 was observed in AN non-myocytes. Cx40 density decreased significantly within myocytes and non-myocytes in AN region and compact AVN of LVD preparations compared to sham (Table 1; Fig. 6). Relative non-myocyte/myocyte associated Cx40 expression remained unchanged during LVD in AN tissue and compact node, while relative Cx43 expression by non-myocytes was significantly increased in AN tissue. A fraction of Cx43 and Cx40 was found to co-localize with both myocytes and non-myocytes, suggesting their presence at points of contact between the two cell types in both the AN region and compact AVN. In LVD animals a significant increase in myocyte–non-myocyte heterocellular connexin localization was observed in the AN region (Cx43: LVD = 11.1 ± 1.9% *vs.* sham = 2.2 ± 0.7% of total Cx43; $p < 0.005$; Cx40: LVD = 6.7 ± 1.0% *vs.* sham = 3.7 ± 0.8% of total Cx40; $p < 0.05$; Table 1).

4. Discussion

The present study provides first evidence of AVN functional and structural remodelling in a rabbit model of CHF, secondary to apical MI. Despite the absence of a direct ischemic insult to the AVN, functional and structural alterations, including increased atrio-ventricular conduction time, prolongation of refractory period, fibrosis and alteration in gap junction levels were observed in the AVN of LVD rabbits. This suggests that AVN remodelling may occur as a pathophysiological response to MI irrespective of where the infarct scar is located.

Initially atrio-ventricular delay was assessed *in vivo via* surface ECG studies. A significant prolongation of the PQ interval by approximately 7 ms (10%) was observed in LVD animals, compared to sham controls. Given that no significant difference in heart rate was observed between the two groups (Fig. 1C), PQ interval prolongation cannot be the result of heart rate-related effects on conduction. The lack of effects on sino-atrial node function was confirmed *via in vitro* studies which demonstrated no difference in the spontaneous sinus cycle length in LVD preparations *versus* sham controls.

A potential contribution to the prolonged PQ interval could stem from longer atrial conduction times, associated with enlarged atria post-MI. Echo based assessment of left atrial dimension (including

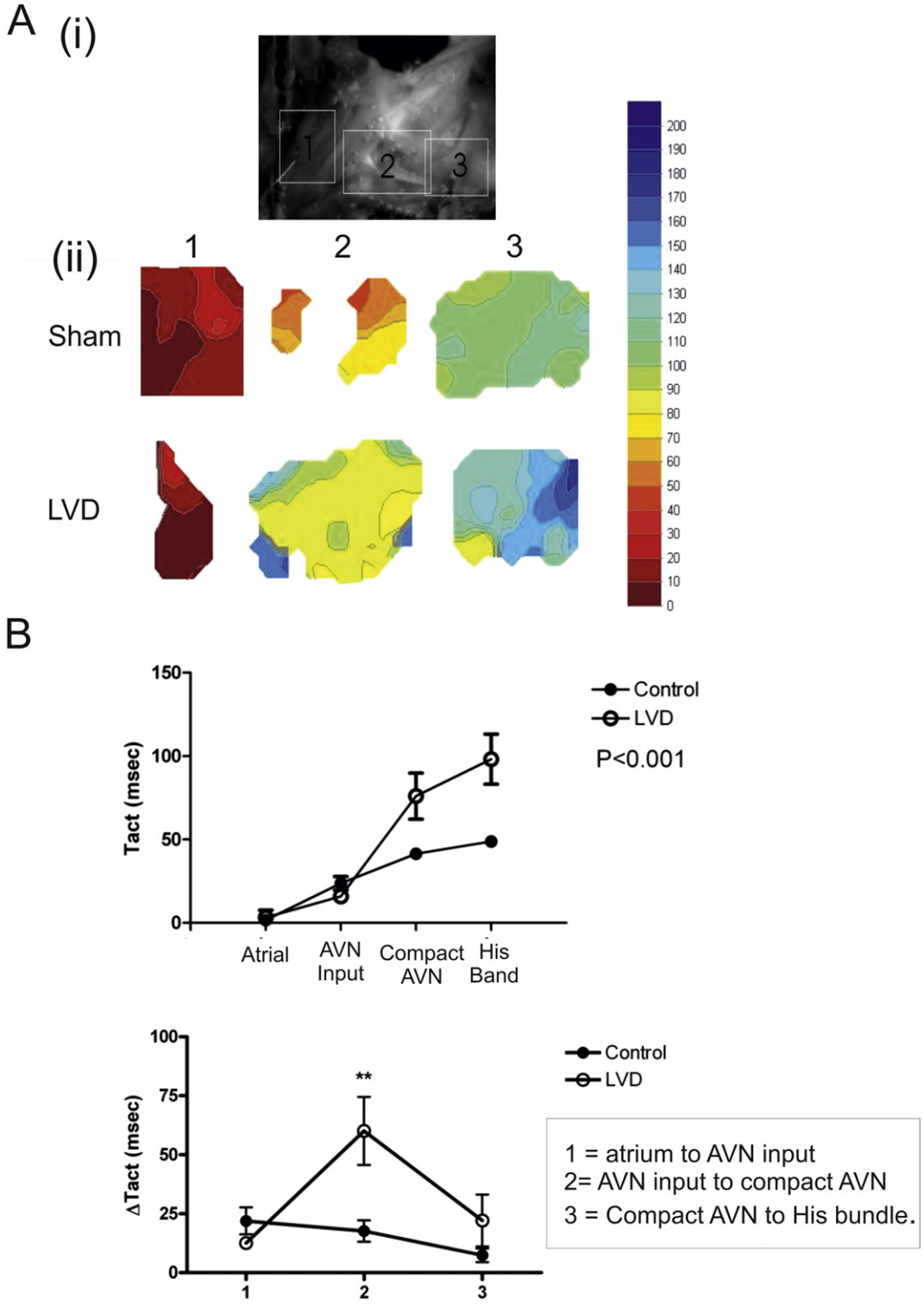

Fig. 5. Regional activation time (T_{act}) measured from optical mapping recordings in isolated AVN preparations. A: Panel (i), CCD image of an isolated AVN preparation, the areas shown correspond to: Region 1: atrium to AVN input; Region 2: AVN input to compact node; Region 3: compact node to His bundle. Panel (ii): isochronal maps of activation showing conduction slowing at region 2 and region 3 in LVD compared to control. B: Time to activation (T_{act}) relative to the atrial electrogram in sham and LVD preparations, and conduction times between adjacent regions (ΔT_{act}). There is significant prolongation of T_{act} in LVD at the compact node and His bundle regions compared to controls (ANOVA $p < 0.001$). This is predominantly a consequence of significant delay in conduction between the AVN input and compact node region. $^{*}p < 0.001$. $n = 4$ sham control/4 LVD.

appendage) indicated a significant enlargement (by approx. 25% of chamber volume) as previously reported in this model [22]. Previous work has reported no change in atrial conduction velocity in the rabbit LVD model [37] which was estimated at approximately 50 cm/s. Based on these measurements, and even allowing for a sino-atrial node to AVN distance of 50% of the maximum atrial circumference, the enlarged atria would cause only a 2–3 ms increase in delay between sino-atrial node and AVN conduction time *i.e.* considerably less than the additional delay measured *in vivo* (7–8 ms).

Further evidence supporting the presence of abnormal conduction inside the AVN in the LVD model comes from intact heart optical mapping studies (Fig. 2). The time to earliest LV epicardial activation during

Table 1
Cx43 and Cx40 density in the atrio-nodal region and compact AVN of LVD and sham hearts.

		Atrio-nodal region				Compact AVN	
		Cx43		Cx40		Cx40	
		Sham $n = 7$	LVD $n = 7$	Sham $n = 7$	LVD $n = 7$	Sham $n = 7$	LVD $n = 7$
Area $\times 10^{-2}$ μm^2 × μm^{-2}	Cx	1.30 ± 0.07	$1.54 \pm 0.06^{*}$	$11.65 \pm 1.5^{\ddagger}$	$4.69 \pm 0.69^{**\ddagger}$	13.61 ± 0.97	$6.24 \pm 0.57^{**}$
	M Cx	1.46 ± 0.08	1.59 ± 0.03	$12.80 \pm 1.56^{\ddagger}$	$5.39 \pm 0.79^{**\ddagger}$	$18.98 \pm 1.14^{\Psi}$	$9.73 \pm 1.13^{**\Psi\Psi}$
	nM Cx	0.52 ± 0.10	$1.40 \pm 0.22^{**}$	$5.02 \pm 0.73^{\ddagger}$	$2.05 \pm 0.27^{*}$	3.63 ± 0.69	$1.37 \pm 0.28^{**\Psi}$
	nM/M	0.34 ± 0.07	$0.85 \pm 0.13^{*}$	0.36 ± 0.03	$0.38 \pm 0.02^{\ddagger}$	$0.18 \pm 0.03^{\Psi\Psi}$	$0.16 \pm 0.02^{\Psi\Psi}$
M-nM Cx(%)		2.18 ± 0.69	$11.08 \pm 1.91^{**}$	3.68 ± 0.80	$6.73 \pm 0.99^{*}$	$7.17 \pm 1.19^{\Psi}$	8.91 ± 0.85

Data obtained from sham and 8 weeks LVD hearts were compared using unpaired *t*-test. Connexin (Cx) density is expressed as area of connexin-related fluorescence per total tissue area (μm^2 × μm^{-2}; Cx) or cell type-specific tissue area (M Cx, nM Cx), and as the ratio of nM/M. M-nM Cx (%) = % of connexin expressed by both myocytes and non-myocytes relative to the total connexin area. Data are presented as mean ± S.E.M. $n = 7$ sham and 7 LVD AVN preparations. $^{*}p < 0.05$ and $^{**}p < 0.005$ *vs.* sham (statistically significant differences).
Cx40 in compact AVN *vs.* atrio-nodal region and atrio-nodal levels of Cx40 *vs.* Cx43 were compared using unpaired *t*-test. $^{\Psi}p < 0.05$ and $^{\Psi\Psi}p < 0.005$ *vs.* Cx40 in atrio-nodal region.
$^{\ddagger}p < 0.001$ *vs.* Cx43 in atrio-nodal region. M: myocytes. nM: non-myocytes.

right atrial pacing was prolonged in LVD rabbits compared to sham controls by approximately 14 ms (16%) (Fig. 2C and D), and this time progressively increased with faster pacing rates (Fig. 2D), characteristic of decremental conduction properties of the AVN. Epicardial activation time was mapped at corresponding sites of healthy and LVD hearts (Fig. 2C), and proximal to the apical MI scar region. Therefore, delayed conduction into or near the scar was not the mechanism of the observed delay.

Furthermore, there was no significant effect on intra-atrial and intra-ventricular conduction, suggesting that an abnormally slow propagation through the AVN is the basis of the delayed LV activation timing in intact hearts with LVD. This was confirmed by measurements from isolated AVN preparations in which the conduction time was measured directly *via* surface electrograms.

Atrio-ventricular conduction was assessed in isolated AVN preparations containing the Triangle of Koch by applying pacing protocols to create atrio-ventricular conduction and refractory curves (Figs. 3 and 4). The results indicate the presence of electrical remodelling in the AVN of LVD rabbits. This manifested as prolongation of the time taken for excitation to propagate between the atrium and the bundle of His (AH interval) at all tested pacing cycle lengths by approximately 15 ms in the LVD group (Fig. 3C). Furthermore, a prolongation of the Wenckebach cycle length by approximately 40 ms was observed in LVD animals compared to sham controls (Fig. 3C). The atrio-

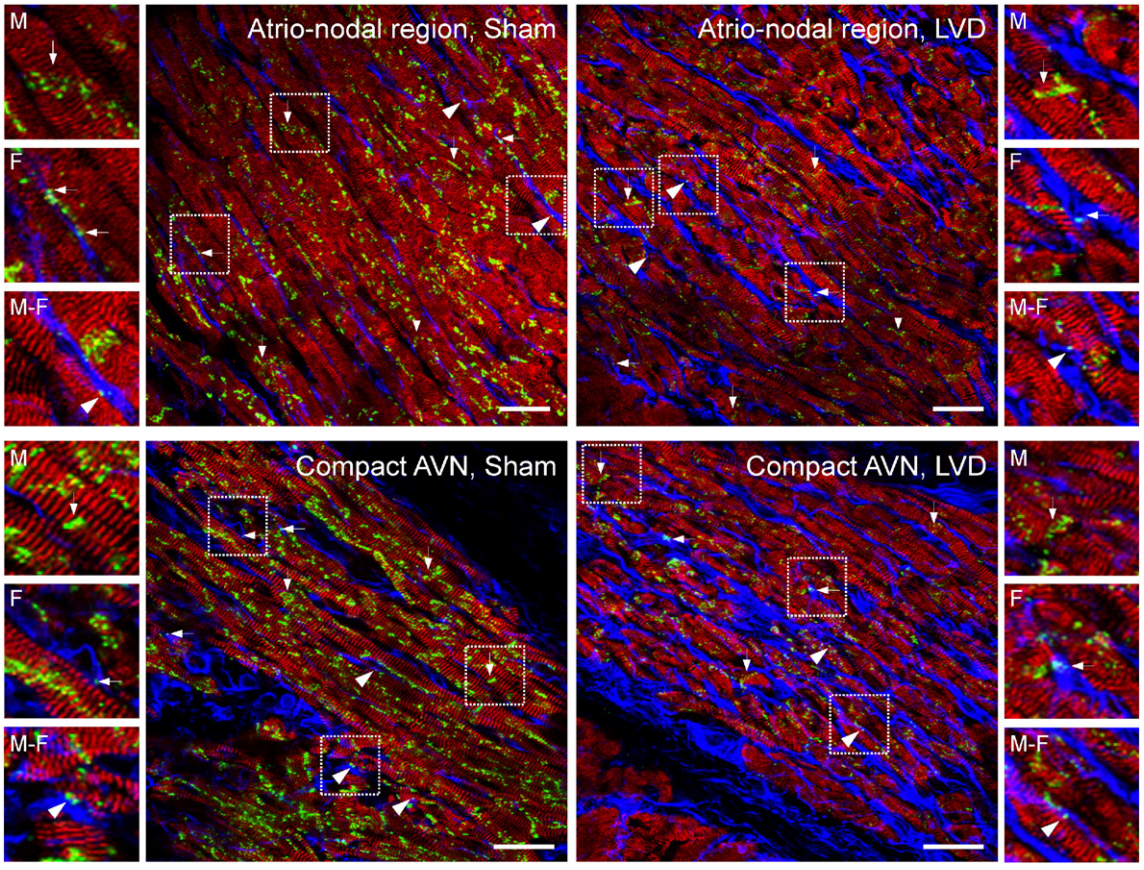

Fig. 6. Triple immunolabelling for myocytes (M; red: anti-myomesin antibody), non-myocytes (based on shape and distribution, fibroblasts: F; blue: anti-vimentin antibody), and Cx40 (green) in sham and LVD rabbit AVN preparations. Different arrow styles indicate Cx colocalization with myocytes only (↓:M), non-myocytes only (←: F), or at heterotypic cell contacts (↗: M-F). Small panels show 2.5 × zoomed views of the areas highlighted by dashed squares in the main images. Scale bars: 30 μm. Note reduction in Cx40 levels in atrio-nodal region and compact AVN of LVD animals *vs.* sham, and increased non-myocyte content.

ventricular delay in isolated AVN preparations was accompanied by an increase in effective and functional refractory periods of the AVN in the absence of change in atrial refractoriness (Fig. 4).

Given the anatomical complexity and heterogeneity of the AVN, the mechanisms by which conduction velocity through the AVN is reduced by LVD are likely to be multiple and complex. In this study, functional measurements of atrio-ventricular conduction in LVD rabbits have shown an increased atrio-ventricular conduction delay by approximately 20% above the normal value, with prolongation of AVN refractory periods by approximately 35 ms. This could be indicative of a disturbance of the electrotonic interaction of cells comprising the AVN, and would have detrimental effects on atrio-ventricular coordination, in particular at high heart rates.

There is considerable diversity in connexin expression within the AVN and adjacent tissue areas, which is thought to be relevant for the heart's complex conduction characteristics [13,38,39]. Studies of Cx40-deficient mice have found evidence of abnormal atrio-ventricular activation delays [40,41]. Another study suggested a link between heart failure and atrio-ventricular conduction defects as a result of alterations in connexin expression in a transgenic mouse model [42]. PR prolongation, observed at 2 weeks of age rapidly progressed into complete AVN block as early as 4 weeks of age. Expression of Cx40 and Cx43 was dramatically decreased in the transgenic heart, which may have contributed to the conduction defects in the transgenic mice. Separately, both fibrosis and connexin down-regulation have been linked to conduction slowing [43,44].

Whether the distribution of gap junctions within the AVN is affected by MI has remained unclear. We therefore explored the hypothesis that in the LVD rabbit model, MI and subsequent heart failure give rise to altered connexin expression in the AVN, which could explain the abnormal atrio-ventricular activation delay observed. Consistent with earlier reports [27,45–47], gap junctions were not limited to myocytes but are also expressed by non-myocytes (Fig. 6). At 8 weeks post-MI, there was notable fibrosis within the AN region and compact AVN of LVD hearts (Fig. 6, Fig. S2). The increased fibrosis within the AN region is accompanied by increased density of Cx43 expression in non-myocytes, but not myocytes. In contrast, Cx40 density was reduced in myocytes of AN and compact AVN tissue in the LVD group (Table 1), which may explain the prolongation of atrio-ventricular conduction in the CHF model.

A fraction of connexins was co-localized with fluorescence indicative of both myocytes and non-myocytes in AN and compact AVN tissue, suggesting the possible presence of heterocellular electrical connections. These were significantly increased in LVD hearts, and, by increasing electrotonic load, could contribute to conduction slowing in the AVN [48,49].

However, the presence of connexin immunostaining at points of contacts between two cell types is not proof of functional coupling, and the possible contribution of heterocellular electrotonic coupling to the functional observation in this model requires further investigations. In a recent study using a rabbit model of cardiac hypertrophy induced by aortic banding and aortic valve damage [11], structural and molecular (mRNA) changes were reported to occur in the AVN. This suggests that remodelling of the electrophysiology of the AVN in response to pathological interventions may involve changes in cellular electrophysiology alongside the changes reported here.

5. Conclusion

This study provides novel evidence to support the hypothesis that prolongation of the PQ interval in a rabbit LVD model is due to remodelling of the AVN in response to remote MI. In the presence of a discrete apical infarct, there was increased AVN fibrosis, connexin remodelling, prolongation of atrio-ventricular conduction, as well as of AVN effective and functional refractory periods. The observed reduction in Cx40 expression and alterations in distribution and density of homo- and hetero-cellular Cx43/Cx40 protein in the AVN may provide a clue to the mechanism of the abnormal delay. Further research is required to pinpoint the dynamic changes in AVN electrophysiology.

6. Limitations

Our immunohistochemical analysis was limited to two connexin isoforms, Cx43 and Cx40. Remodelling of the low-conductivity Cx45 isoform, also present in the AVN, could further contribute to the atrio-ventricular conduction delay observed in this study. Unfortunately we were unable to obtain reliable Cx45 staining for quantification, using currently available commercial Cx45 antibodies. Future studies involving genetic manipulation and/or labelling of connexins may hold the key to a fuller understanding of the contribution of the individual connexin isoform to AVN function and dysfunction.

Supplementary data to this article can be found online at http://dx.doi.org/10.1016/j.yjmcc.2016.03.011.

Disclosures

None.

Acknowledgements

Financially supported by the British Heart Foundation (FS/05/010/18435 and FS/02/018/13463) and the European Research Council (AdG CardioNECT). PC acknowledges support from the UK Physiological Society.

References

[1] C. Alonso, C. Leclercq, F. Victor, H. Mansour, C. de Place, D. Pavin, et al., Electrocardiographic predictive factors of long-term clinical improvement with multisite biventricular pacing in advanced heart failure, Am. J. Cardiol. 84 (1999) 1417–1421.
[2] D.M. Gilligan, D. Sargent, V. Ponnathpur, D. Dan, J.S. Zakaib, K.A. Ellenbogen, Echocardiographic atrioventricular interval optimization in patients with dual-chamber pacemakers and symptomatic left ventricular systolic dysfunction, Am. J. Cardiol. 91 (2003) 629–631.
[3] R. Schoeller, D. Andresen, P. Buttner, K. Oezcelik, G. Vey, R. Schroder, First- or second-degree atrioventricular block as a risk factor in idiopathic dilated cardiomyopathy, Am. J. Cardiol. 71 (1993) 720–726.
[4] W. Shamim, D.P. Francis, M. Yousufuddin, S. Varney, M.F. Pieopli, S.D. Anker, et al., Intraventricular conduction delay: a prognostic marker in chronic heart failure, Int. J. Cardiol. 70 (1999) 171–178.
[5] W. Shamim, M. Yousufuddin, M. Cicoria, D.G. Gibson, A.J. Coats, M.Y. Henein, Incremental changes in QRS duration in serial ECGs over time identify high risk elderly patients with heart failure, Heart 88 (2002) 47–51.
[6] W.T. Abraham, Rationale and design of a randomized clinical trial to assess the safety and efficacy of cardiac resynchronization therapy in patients with advanced heart failure: the Multicenter InSync Randomized Clinical Evaluation (MIRACLE), J. Card. Fail. 6 (2000) 369–380.
[7] W.T. Abraham, W.G. Fisher, A.L. Smith, D.B. Delurgio, A.R. Leon, E. Loh, et al., Cardiac resynchronization in chronic heart failure, N. Engl. J. Med. 346 (2002) 1845–1853.
[8] D.J. Bradley, E.A. Bradley, K.L. Baughman, R.D. Berger, H. Calkins, S.N. Goodman, et al., Cardiac resynchronization and death from progressive heart failure: a meta-analysis of randomized controlled trials, JAMA 289 (2003) 730–740.
[9] M. Gasparini, M. Mantica, P. Galimberti, U. La Marchesina, M. Manglavacchi, F. Faletra, et al., Optimization of cardiac resynchronization therapy: technical aspects, Eur. Heart J. Suppl. 4 (D82–D7) (2002).
[10] Z.I. Whinnett, J.E. Davies, K. Willson, C.H. Manisty, A.W. Chow, R.A. Foale, et al., Haemodynamic effects of changes in atrioventricular and interventricular delay in cardiac resynchronisation therapy show a consistent pattern: analysis of shape, magnitude and relative importance of atrioventricular and interventricular delay, Heart 92 (2006) 1628–1634.
[11] T. Nikolaidou, X.J. Cai, R.S. Stephenson, J. Yanni, T. Lowe, A.J. Atkinson, et al., Congestive heart failure leads to prolongation of the PR interval and atrioventricular junction enlargement and ion channel remodelling in the rabbit, PLoS One 10 (2015), e0141452.
[12] H. Dobrzynski, R.H. Anderson, A. Atkinson, Z. Borbas, A. D'Souza, J.F. Fraser, et al., Structure, function and clinical relevance of the cardiac conduction system, including the atrioventricular ring and outflow tract tissues, Pharmacol. Ther. 139 (2013) 260–288.
[13] I.P. Temple, S. Inada, H. Dobrzynski, M.R. Boyett, Connexins and the atrioventricular node, Heart Rhythm. 10 (2013) 297–304.
[14] T.N. Mazgalev, D.R. Van Wagoner, I.R. Efimov, Mechanisms of AV nodal excitability and propagation, Cardiac Electrophysiology: From Cell to Bedside, W.B. Saunders Co. 1999, pp. 196–205 Zipes & Jalife.

[15] T.N. James, Structure and function of the sinus node, AV node and his bundle of the human heart: part II–function, Prog. Cardiovasc. Dis. 45 (2003) 327–360.
[16] J. Merideth, C. Mendez, W.J. Mueller, G.K. Moe, Electrical excitability of atrioventricular nodal cells, Circ. Res. 23 (1968) 69–85.
[17] J. Billette, S. Nattel, Dynamic behavior of the atrioventricular node: a functional model of interaction between recovery, facilitation, and fatigue, J. Cardiovasc. Electrophysiol. 5 (1994) 90–102.
[18] F.L. Burton, A.R. McPhaden, S.M. Cobbe, Ventricular fibrillation threshold and local dispersion of refractoriness in isolated rabbit hearts with left ventricular dysfunction, Basic Res. Cardiol. 95 (2000) 359–367.
[19] S.E. Litwin, J.H. Bridge, Enhanced Na^+-Ca^{2+} exchange in the infarcted heart. Implications for excitation-contraction coupling, Circ. Res. 81 (1997) 1083–1093.
[20] K.W. Mahaffey, T.E. Raya, G.D. Pennock, E. Morkin, S. Goldman, Left ventricular performance and remodeling in rabbits after myocardial infarction. Effects of a thyroid hormone analogue, Circulation 91 (1995) 794–801.
[21] M.A. McIntosh, S.M. Cobbe, G.L. Smith, Heterogeneous changes in action potential and intracellular Ca^{2+} in left ventricular myocyte sub-types from rabbits with heart failure, Cardiovasc. Res. 45 (2000) 397–409.
[22] G.A. Ng, S.M. Cobbe, G.L. Smith, Non-uniform prolongation of intracellular Ca^{2+} transients recorded from the epicardial surface of isolated hearts from rabbits with heart failure, Cardiovasc. Res. 37 (1998) 489–502.
[23] M.P. Pye, S.M. Cobbe, Arrhythmogenesis in experimental models of heart failure: the role of increased load, Cardiovasc. Res. 32 (1996) 248–257.
[24] M.P. Pye, M. Black, S.M. Cobbe, Comparison of in vivo and in vitro haemodynamic function in experimental heart failure: use of echocardiography, Cardiovasc. Res. 31 (1996) 873–881.
[25] S.F. Mironov, F.J. Vetter, A.M. Pertsov, Fluorescence imaging of cardiac propagation: spectral properties and filtering of optical action potentials, Am. J. Physiol. Heart Circ. Physiol. 291 (2006) H327–H335.
[26] N.L. Walker, F.L. Burton, S. Kettlewell, G.L. Smith, S.M. Cobbe, Mapping of epicardial activation in a rabbit model of chronic myocardial infarction, J. Cardiovasc. Electrophysiol. 18 (2007) 862–868.
[27] P. Camelliti, C.R. Green, I. LeGrice, P. Kohl, Fibroblast network in rabbit sinoatrial node: structural and functional identification of homogeneous and heterogeneous cell coupling, Circ. Res. 94 (2004) 828–835.
[28] P. Camelliti, S.A. Al-Saud, R.T. Smolenski, S. Al-Ayoubi, A. Bussek, E. Wettwer, et al., Adult human heart slices are a multicellular system suitable for electrophysiological and pharmacological studies, J. Mol. Cell. Cardiol. 51 (2011) 390–398.
[29] R.C. Myles, F.L. Burton, S.M. Cobbe, G.L. Smith, Alternans of action potential duration and amplitude in rabbits with left ventricular dysfunction following myocardial infarction, J. Mol. Cell. Cardiol. 50 (2011) 510–521.
[30] F.R. Quinn, S. Currie, A.M. Duncan, S. Miller, R. Sayeed, S.M. Cobbe, et al., Myocardial infarction causes increased expression but decreased activity of the myocardial Na^+-Ca^{2+} exchanger in the rabbit, J. Physiol. 553 (2003) 229–242.
[31] G.A. Ng, M.N. Hicks, S.M. Cobbe, G.L. Smith, Depressed inotropic response to increased preload in rabbit hearts with left-ventricular dysfunction induced by chronic myocardial infarction, Pflugers Arch. 444 (2002) 513–522.
[32] P. Neary, A.M. Duncan, S.M. Cobbe, G.L. Smith, Assessment of sarcoplasmic reticulum Ca^{2+} flux pathways in cardiomyocytes from rabbits with infarct-induced left-ventricular dysfunction, Pflugers Arch. 444 (2002) 360–371.
[33] P. Neary, S.M. Cobbe, G.L. Smith, Reduced sarcoplasmic reticulum Ca^{2+} release in rabbits with left ventricular dysfunction, Ann. N. Y. Acad. Sci. 853 (1998) 338–340.
[34] C. Mendez, G.K. Moe, Demonstration of a dual A-V nodal conduction system in the isolated rabbit heart, Circ. Res. 19 (1966) 378–393.
[35] V. Nikolski, I. Efimov, Fluorescent imaging of a dual-pathway atrioventricular-nodal conduction system, Circ. Res. 88 (2001) E23–E30.
[36] V.P. Nikolski, S.A. Jones, M.K. Lancaster, M.R. Boyett, I.R. Efimov, Cx43 and dual-pathway electrophysiology of the atrioventricular node and atrioventricular nodal reentry, Circ. Res. 92 (2003) 469–475.
[37] S. Kettlewell, F.L. Burton, G.L. Smith, A.J. Workman, Chronic myocardial infarction promotes atrial action potential alternans, afterdepolarizations, and fibrillation, Cardiovasc. Res. 99 (2013) 215–224.
[38] S.R. Coppen, N.J. Severs, Diversity of connexin expression patterns in the atrioventricular node: vestigial consequence or functional specialization? J. Cardiovasc. Electrophysiol. 13 (2002) 625–626.
[39] H. Dobrzynski, V.P. Nikolski, A.T. Sambelashvili, I.D. Greener, M. Yamamoto, M.R. Boyett, et al., Site of origin and molecular substrate of atrioventricular junctional rhythm in the rabbit heart, Circ. Res. 93 (2003) 1102–1110.
[40] A.M. Simon, D.A. Goodenough, D.L. Paul, Mice lacking connexin40 have cardiac conduction abnormalities characteristic of atrioventricular block and bundle branch block, Curr. Biol. 8 (1998) 295–298.
[41] W. Zhu, S. Saba, M.S. Link, E. Bak, M.K. Homoud, N.A. Estes 3rd, et al., Atrioventricular nodal reverse facilitation in connexin40-deficient mice, Heart Rhythm. 2 (2005) 1231–1237.
[42] H. Kasahara, H. Wakimoto, M. Liu, C.T. Maguire, K.L. Converso, T. Shioi, et al., Progressive atrioventricular conduction defects and heart failure in mice expressing a mutant Csx/Nkx2.5 homeoprotein, J. Clin. Invest. 108 (2001) 189–201.
[43] Y. Xie, A. Garfinkel, P. Camelliti, P. Kohl, J.N. Weiss, Z. Qu, Effects of fibroblast-myocyte coupling on cardiac conduction and vulnerability to reentry: a computational study, Heart Rhythm. 6 (2009) 1641–1649.
[44] R.M. Shaw, Y. Rudy, Ionic mechanisms of propagation in cardiac tissue. Roles of the sodium and L-type calcium currents during reduced excitability and decreased gap junction coupling, Circ. Res. 81 (1997) 727–741.
[45] P. Camelliti, G.P. Devlin, K.G. Matthews, P. Kohl, C.R. Green, Spatially and temporally distinct expression of fibroblast connexins after sheep ventricular infarction, Cardiovasc. Res. 62 (2004) 415–425.
[46] E.C. Goldsmith, A. Hoffman, M.O. Morales, J.D. Potts, R.L. Price, A. McFadden, et al., Organization of fibroblasts in the heart, Dev. Dyn. 230 (2004) 787–794.
[47] P. Camelliti, C.R. Green, P. Kohl, Structural and functional coupling of cardiac myocytes and fibroblasts, Adv. Cardiol. 42 (2006) 132–149.
[48] P. Kohl, P. Camelliti, Fibroblast-myocyte connections in the heart, Heart Rhythm. 9 (2012) 461–464.
[49] P. Kohl, R.G. Gourdie, Fibroblast-myocyte electrotonic coupling: does it occur in native cardiac tissue? J. Mol. Cell. Cardiol. 70 (2014) 37–46.